*Article*

# Structural Engineering of Photocatalytic ZnO-SnO$_2$-Fe$_2$O$_3$ Composites

Larissa L. Khomutinnikova [1], Sergey K. Evstropiev [1,2,*], Dmitry P. Danilovich [2], Igor K. Meshkovskii [1] and Dmitry V. Bulyga [1,*]

1   Technical Physics Department, ITMO University, Saint-Petersburg 197101, Russia
2   Department of Chemistry of Compounds and Materials, Saint-Petersburg State Technological Institute, Technical University, Saint-Petersburg 190013, Russia
*   Correspondence: evstropiev@bk.ru (S.K.E.); dmbulyga@yandex.ru (D.V.B.)

**Abstract:** The ZnO-SnO$_2$-Fe$_2$O$_3$ composites containing flower-like particles were prepared by the non-isothermal polymer-salt method. Thermochemical processes proceeding during composites synthesis was studied by DTA/TG method. The structure and morphology of obtained composites were studied by the SEM and XRD analysis. Prepared composites containing small amounts of SnO$_2$ and Fe$_2$O$_3$ demonstrate the high adsorption and photodecomposition of the organic dye Rhodamine 6G in its solutions. Obtained materials show the ability of the photogeneration of the chemically active singlet oxygen under the visible irradiation. The synergistic effect of the flower structure and Fe$_2$O$_3$ doping can significantly improve the photocatalytic and adsorption activities.

**Keywords:** heterostructure; photocatalysis; ZnO; adsorption; flower-like

## 1. Introduction

The research and development of new effective photocatalytic materials are the subject of numerous and intensive studies being carried out all over the world. It is known that materials based on zinc oxide are one of the most efficient photocatalysts [1–19].

The structural engineering is the effective way to the fabrication of different materials with high photocatalytic properties [1–3,16,20–24]. This approach includes different aspects of the materials structure optimization: the preparation of nanomaterials with the high specific surface area and special shapes of nanoparticles (nanorods [25,26], nanowires [5,15,27], "flowers" [14,28–31], etc.); the control of structural defects [1,5,24,32–34]; the application of porous matrixes [23,28,35,36]; materials doping [2,7–9,26,28,37,38] and others.

It is well-known that photocatalytic and bactericidal properties of ZnO-based materials can be enhanced by the small addition of some modifying components (Mn [2], Sn [11], Ag [28], Co [37], Al [39]). This addition can decrease the size of ZnO crystals and increase their specific surface area [11,37,39,40], prevent the recombination of photogenerated electron-hole pairs [7,9–12], widening the spectral diapason of the radiation effectively exciting the photocatalysts [2,7,28,37].

The morphology engineering promotes the significant improvement of photocatalytic properties of ZnO-based materials [2,3,17]. High photocatalytic properties were demonstrated by materials having high specific surface areas and consisting of ZnO particles having specific shapes of wires [5,15], rods [18,34], flowers [25,28,31], cones [4], sheets [10,29], porous nanospheres [23], etc.

The method used for the fabrication of ZnO-based materials affect strongly their morphology and photocatalytic characteristics [30,40]. Different liquid-phase methods are widely used for their synthesis: hydrothermal method [5,6,25,28,41], electrodeposition [6], sol-gel [30,40], precipitation [2,30,42], polymer-salt method [11,13,40,43], microwave synthesis [3].

1-D nanostructures (nanowires; nanorods), which are known to have a high surface-to-volume ratio, with a high surface defect density, are very efficient photocatalysts [5,15,27].

Synthesis of these structures often proceeds through the heterogeneous crystallization of ZnO on preliminary prepared seeds [5,6,44]. So, photocatalytic ZnO nanowires were grown by hydrothermal [5,6,41] and electrodeposition [6] methods on the substrates preliminarily covered by ZnO nanoparticles. In [34], ZnO nano-/micro-rods were synthesized by the hydrothermal route with the presence of polyvinylpyrrolidone (PVP).

The hydrothermal method was applied also for the fabrication of flower-like ZnO structures using as surfactants cetyl-trimethyl-ammonium bromide [25] and sodium dodecel sulfate [29]. In [28,30], flower-like ZnO structures were synthesized by the hydrothermal method without any surfactants. Sol-gel-based hydrothermal method was used in [16] for the synthesis of 3D flower-like ZnO microstructures composed of nanosheets for photocatalytic applications. Flower-like composite ZnO/Au and ZnO/Ag structures were prepared by the liquid deposition method in [45]. The liquid-phase synthesis and applications of 3D ZnO hierarchical nanostructures were described in detail in [46].

The formation of ZnO wires, rods, and flower-like structures having high photocatalytic properties often proceeds through the heterogeneous crystallization of zinc oxide [30,45]. Different preliminary formed nanoparticles (such as modifying additions (Au or Ag nanoparticles [45]), so as firstly formed ZnO nanoparticles [47]) can play the role of seeds for the main part of ZnO crystallization.

Polymer-salt method based on the application of composite solutions containing metals salts and organic polymer is used for the preparation of nanopowders as transparent coatings having high photocatalytic properties [11,13,40,43]. Composite solutions are subjected to drying and the following thermal treatment for the full decomposition of organics and metals salts and the formation of metal oxides nanoparticles.

This method was successfully applied for the fabrication of multicomponent photocatalytic materials [40] and semiconductor heterostructures [11,13]. Different metals salts can decompose at various temperatures during non-isothermal thermal treatment. In this case, the heterogeneous crystallization can proceed and form particles of the one metal oxide that can play the role of seeds for the crystallization of other part of the material. It was found [48] that kinetics features of the thermal precursor decomposition and oxidation can determine the morphology of the obtained oxide nanostructure.

In this work we synthesized $ZnO$-$SnO_2$-$Fe_2O_3$ composites by the non-isothermal polymer-salt method and studied their structure, morphology, and different properties.

## 2. Materials and Methods

The polymer-salt method previously described in [11,13,40] was used for the composite synthesis. Aqueous solutions of $Zn(NO_3)_2$, $SnCl_2$, and $FeCl_3$ in pre-determined volumes were mixed with the solution of high-molecular polyvinylpyrrolidone (PVP, Mw = 1,300,000; Sigma Aldrich, St. Louis, MO, USA) in ethanol. Prepared mixed solutions were dried in air atmosphere at 70 °C, and then the obtained organic-salt composites were calcined at 550 °C in the electric laboratory furnace. Chemical compositions of prepared solutions are given in Table 1.

**Table 1.** Chemical compositions of prepared solutions and oxide composites.

| Sample | Chemical Compositions, mol. % | | | | | | | | |
| | Solutions | | | | | | Composites | | |
| | $H_2O$ | Ethanol | $Zn(NO_3)_2$ | $SnCl_2$ | $FeCl_3$ | PVP | ZnO | $SnO_2$ | $Fe_2O_3$ |
|---|---|---|---|---|---|---|---|---|---|
| **1** | 47.62 | 47.62 | 2.26 | 0.12 | - | 2.38 | 95.0 | 5.0 | - |
| **2** | 47.62 | 47.62 | 2.30 | 0.07 | 0.01 | 2.38 | 96.5 | 3.0 | 0.5 |
| **3** | 47.62 | 47.62 | 2.26 | 0.07 | 0.05 | 2.38 | 95.0 | 3.0 | 2.0 |
| **4** | 47.62 | 47.62 | 2.07 | 0.07 | 0.24 | 2.38 | 87.0 | 3.0 | 10.0 |

Nominal chemical compositions.

The thermal evolution of dried PVP-salts composites was studied by DTA-TG method using a STA 449F1 Jupiter (Nietzsche) device. SEM analysis using the instrument TESCAN MIRA3 was applied to study the morphology of the obtained composites.

It is known [49] that chemically active singlet oxygen demonstrates characteristic photoluminescence in NIR spectral range ($\lambda_{max.}$ = 1270 nm) under the external irradiation. In this work we study the photogeneration of singlet oxygen by preparing composites under the visible irradiation using the experimental setup described in detail in [50]. The luminescence excitation was carried out using LED (HPR40E set) ($\lambda_{max}$ = 405 nm; power density 0.90 W/cm$^2$).

To study the adsorption and photocatalytic properties of composites, we used organic dye Rhodamine 6G, whose properties are well studied [51]. The solutions of this dye in ethanol (C = $10^{-5}$ M; volume 5 mL) and powders samples (0.1 g) were used in photocatalytic experiments. Dye solutions containing powder composite additions were subjected to the radiation of HPR40E ($\lambda_{ex.}$ = 370 nm). Dye concentrations in solutions were obtained by the measurements of their adsorption spectra using Perkin-Elmer Lambda 650 dual-beam UV-visible spectrophotometer.

## 3. Results

### 3.1. DTA/TG

Figure 1 shows the data of DTA/TG analysis of dried PVP/salts composites. During the thermal treatment all samples are decomposed with significant weight losses and exothermic effects. Weight changes in the observed samples at relatively low temperatures (T < 200 °C) are determined by removing water. The heating of PVP-salts composites to higher temperatures leads to their structural transformations which are completed at 550 °C with oxide formation.
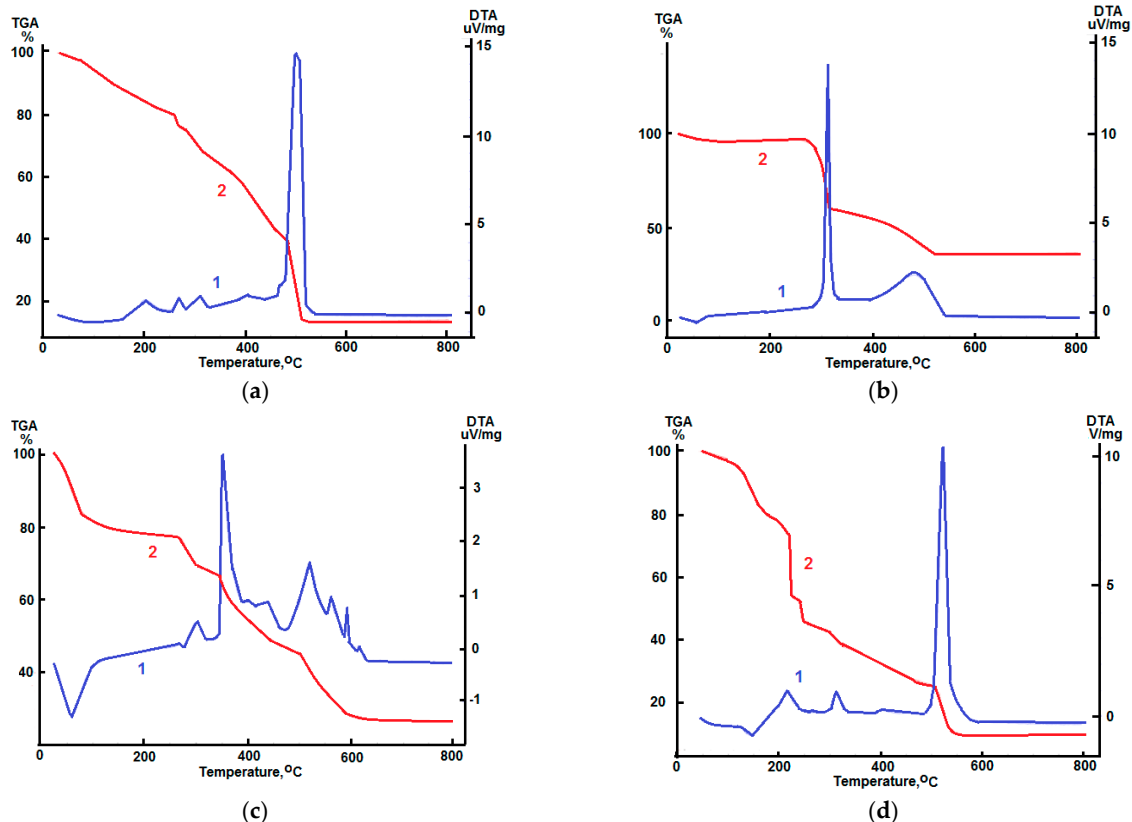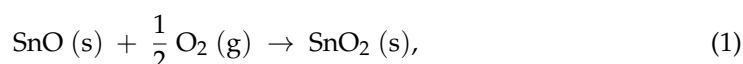


**Figure 1.** Thermal evolution of PVP-salts composite materials. (**a**) PVP-Zn(NO$_3$)$_2$; (**b**) PVP-SnCl$_2$; (**c**) PVP-FeCl$_3$; (**d**) PVP-Zn(NO$_3$)$_2$-SnCl$_2$-FeCl$_3$. 1—DTA curves; 2—TG curves.

The intensive exothermal peak and corresponding weight losses are observed at ~500 °C in DTA/TG plot of PVP/Zn(NO$_3$)$_2$ composite. This phenomenon is related to the nitrate anions and PVP decomposition and ZnO particles formation. Similar results of DTA/TG analysis of PVP/Zn(NO$_3$)$_2$ and PVP/Zn(NO$_3$)$_2$/SnCl$_2$ composites were reported earlier in [13]. Comparing the experimental data given in [13] with the results shown in Figure 1d, we can conclude that the addition of small amounts of FeCl$_3$ has no significant influence on the behavior of the thermal evolution of PVP/Zn(NO$_3$)$_2$/SnCl$_2$ composites.

Thermal evolution of tin (II) oxyhydroxide Sn$_6$O$_4$(OH)$_4$ and the subsequent oxidation to tin (IV) oxide SnO$_2$ during thermal treatment in the air atmosphere was studied in [48]. The oxidation of SnO and the formation of SnO$_2$ particles, according to chemical reaction is [52]:

$$\text{SnO (s)} + \frac{1}{2}\,\text{O}_2\,\text{(g)} \rightarrow \text{SnO}_2\,\text{(s)}, \tag{1}$$

proceeding in the temperature diapason 300 ÷ 350 °C [48]. It is worth to notice that obtained DTA/TG data (Figure 1b) agree with the behavior of the thermal evolution of tin oxide materials described in [48].

Obtained DTA/TG curves suggest the stepped behavior of the thermal evolution of PVP/FeCl$_3$ composite (Figure 1c). The process of thermal decomposition of FeCl$_3$ and synthesis of Fe$_2$O$_3$ crystals proceeds through the formation of numerous intermediate compounds (Fe(OH)$_2$Cl; FeOCl; β-FeOOH) [53].

The presence of PVP in the PVP/salts composites determines additional weight losses and exothermic effects due to the polymer oxidation and decomposition at the diapason 200 ÷ 500 °C [43,54,55]. The heating of composites simultaneously containing metal nitrates and PVP leads to the exothermic oxidation–reduction reaction accompanying the formation of gaseous products [25,34]. This phenomena inputs some increase in observed exothermic effects in DTA curves (Figure 1a,d).

Thus, DTA/TG data show that the heating of PVP-salts composites is accompanied by significant weight losses and exothermal effects that are related to the material structural transformation. The thermal treatment of these composites to 550 °C leads to the full decomposition of salts and PVP. Obtained data fully agree to previously reported results [13,43,48,52–55] and indicate that the small addition of Sn and Fe compounds have no remarkable influence on the thermal evolution of PVP-Zn(NO$_3$)$_2$ composite.

Thus, the experimental data of DTA/TG analysis indicate that structural transformations (salts and PVP decomposition; different oxide crystals formation) proceed at different temperatures in the wide temperature diapason (300 ÷ 550 °C) during the non-isothermal precursors heating.

### 3.2. XRD Analysis

As shown in Figure 2, the crystal structures of formed composites were investigated by XRD. The most intensive peaks in all diffraction patterns correspond to the hexagonal wurtzite ZnO phase (PDF#36-1451) that is related to chemical compositions of prepared samples. The ratios between the measured relative intensities of diffraction peaks of ZnO crystals are close to the standard data (PDF#36-1451) for all samples that indicate the absence of texture in their structures.

Regarding samples **2–4**, after annealing at 550 °C in air, the measurements showed diffraction peaks at 26.6°, 33.9°, and 38.3°, which correspond to the (110), (101), and (111) planes of cassiterite structure of SnO$_2$ (PDF#41-1445), respectively. Beside tetragonal cassiterite crystals, the addition of tin compound led to the formation of zinc stannate (Zn$_2$SnO$_4$) crystals which have high photocatalytic and bactericidal properties [56,57] and are more stable against acidic dyes than ZnO [58].
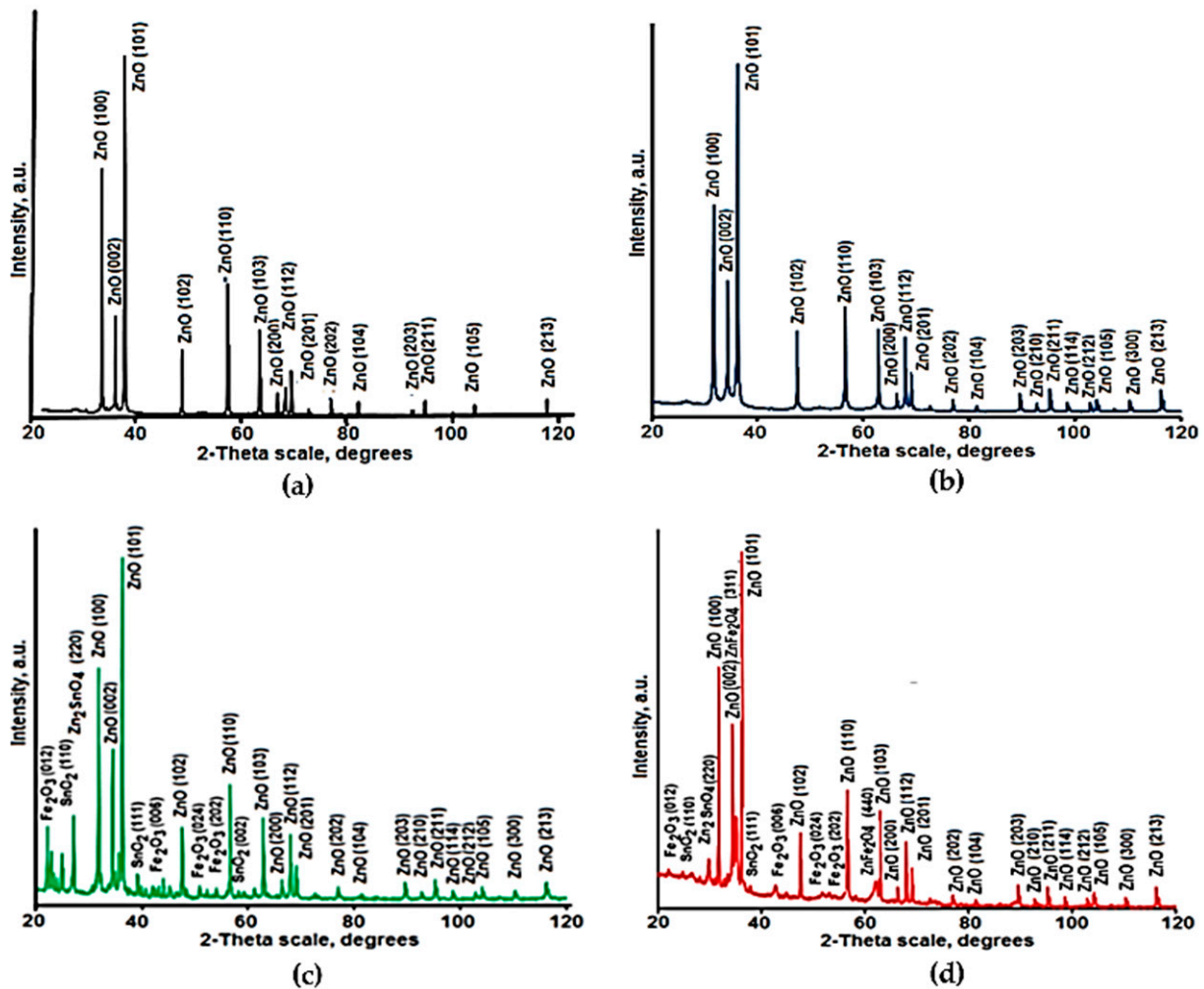
**Figure 2.** XRD patterns of samples **1** (**a**), **2** (**b**), **3** (**c**), **4** (**d**).

The peaks of $ZnFe_2O_4$ crystals (JCPDS card 79-1150) are observed in XRD pattern of the sample **4** containing 10.0 mol.% $Fe_2O_3$. It is worth to notice that these crystals demonstrate photocatalytic properties also [59].

Thus, XRD data indicate the formation of many different photoactive crystals in obtained $ZnO-SnO_2-Fe_2O_3$ composites. The main crystal phase of all composites is hexagonal ZnO crystals that corresponds to the chemical composition of prepared materials (Table 1).

*3.3. SEM Analysis*

Figure 3 demonstrates SEM photo of samples **1**, **3**, and **4** calcined at 550 °C. The structure of samples **3** and **4** contains flower-like aggregates, consisting of hexagonal ZnO rods (Figure 3d) growth from the one seed (Figure 3b,d). Similar morphology was observed earlier in [45] in ZnO/Ag and ZnO/Au composite materials. In these materials the heterogeneous crystallization of ZnO crystals occurred on preliminary formed metallic (Ag, Au) nanoparticles. In pure ZnO coatings prepared by the polymer-salt method in [60], the formation of flower-like aggregates was not observed and materials consisted of small uniform spherical ZnO nanoparticles. Figure 3a shows that flower-like aggregates are also absent in the structure of the prepared powder $ZnO-SnO_2$ (sample **1**).
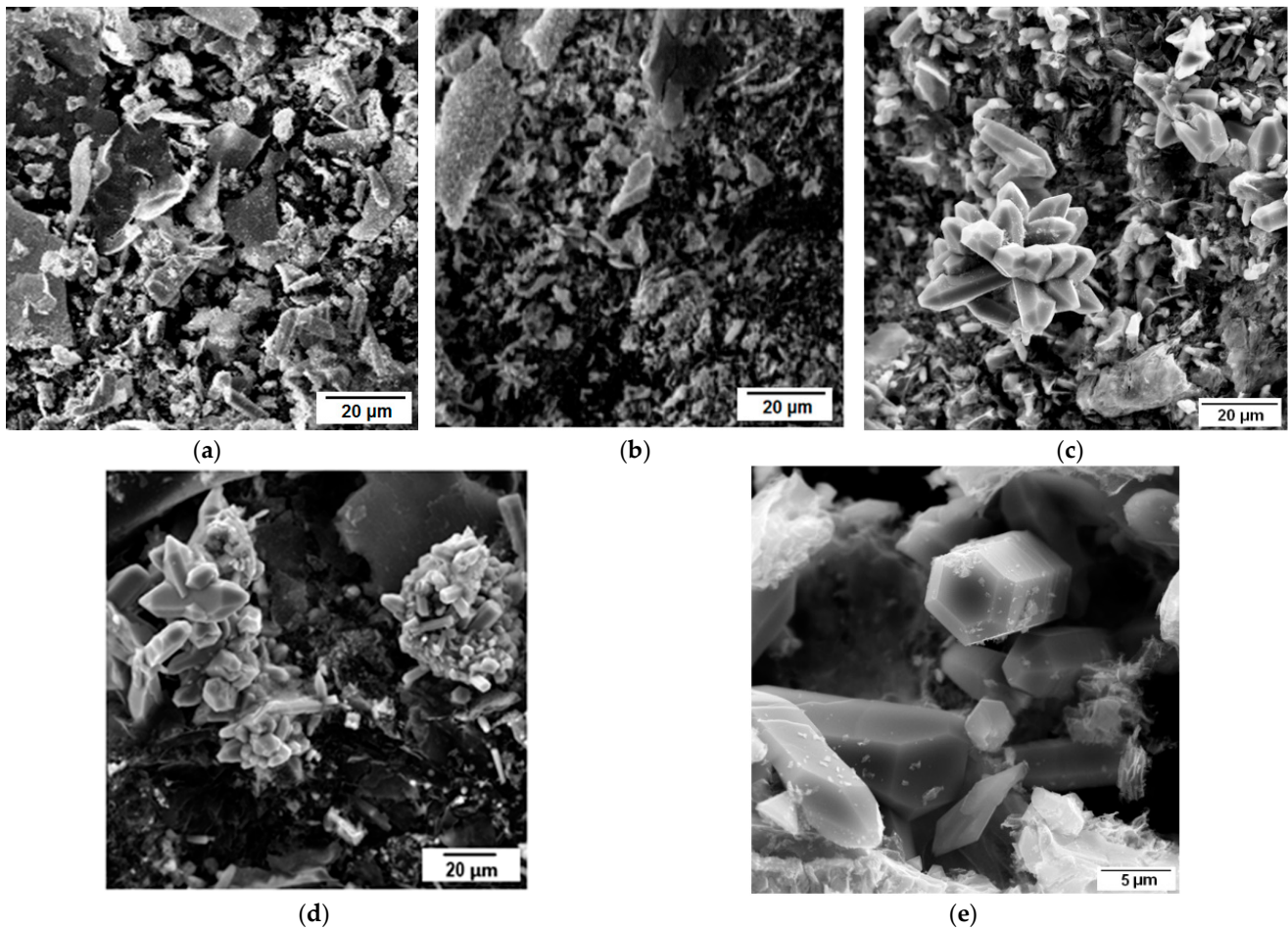
**Figure 3.** SEM photo of samples **1** (**a**), **2** (**b**) **3** (**c**,**e**) and **4** (**d**).

Besides these flower-like aggregates, numerous sub-micron particles are present in the composite structures. SEM photo shows that composites have disperse structures that can provide high photocatalytic activity of these materials.

*3.4. Photoluminescence Properties and Singlet Oxygen Photogeneration*

Luminescence properties of ZnO-based materials in the visible spectral range are often related to intrinsic defects of ZnO crystals (oxygen vacancies, Zn interstitials, and others) [61–63]. These defects can play an important role in photocatalytic processes [64,65] and their formation in crystal structures of photocatalysts is the subject of many studies [61–66].

Figure 4a shows photoluminescence spectra of powder sample **3** in the visible diapason. Numerous luminescence peaks are observed in these spectra. Intensive peaks observed in the blue part of luminescence spectra ($\lambda_{max}$ = 420, 440 and 455 nm) can be assigned to structural defects of ZnO (Zn interstitials [62,66]) and $SnO_2$ crystals [67,68]). The luminescence of ZnO-$SnO_2$ nanocomposites was observed in the blue spectral region in [13]. The luminescence bands in the green-yellow spectral range (525 ÷ 575 nm) correspond to oxygen vacancies in ZnO [63] or $SnO_2$ [69] crystals. Obtained results suggest that prepared composites contain different structural defects modifying the electronic structure of materials and determining their luminescent properties in the visible spectral range.
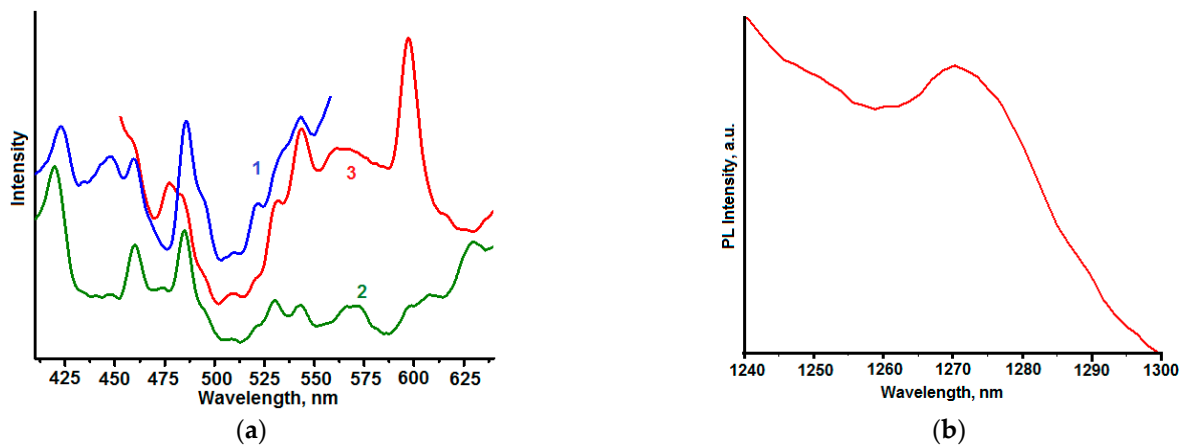
**Figure 4.** (**a**) Photoluminescence spectra of powder sample **3** in the visible diapason. Excitation wavelengths, nm: 300 (curve 1); 350 (curve 2); 400 (curve 3). (**b**) Photoluminescence spectra of powder sample **3** in NIR spectral range. Excitation wavelength 405 nm.

Reactive oxygen species (ROS) play an important role in photocatalytic processes [13,24,49,70–73]. Figure 4 shows the photoluminescence spectrum of powder sample **3** in NIR spectral range. The luminescent band ($\lambda_{max}$ = 1270 nm) which is characteristic of the $^1\Delta_g$-$^3\Sigma_g$ electronic transition of singlet oxygen [49] is observed in this spectrum.

### 3.5. Photocatalytic Properties

Orange-colored solutions of Rhodamine 6G become colorless under the action of UV radiation, and the addition of synthesized powders to them significantly accelerates this process. Figure 5a illustrates changes in absorption spectra of a dye solution containing powder sample **2** under UV irradiation.
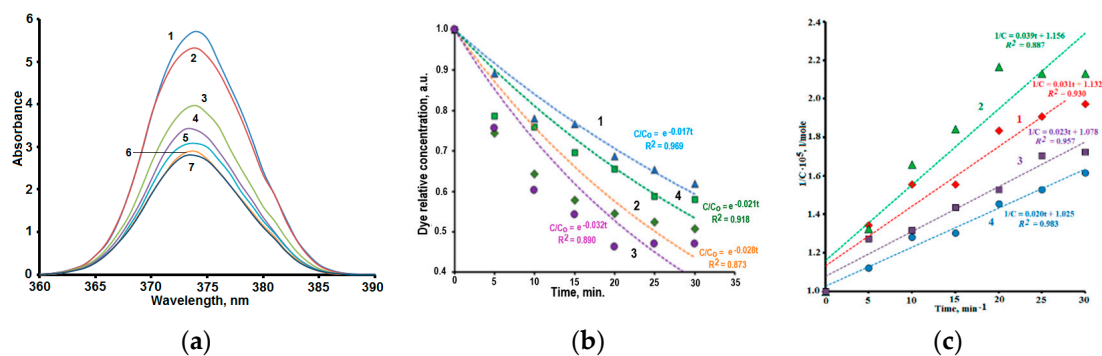


**Figure 5.** (**a**) Changes in absorption spectra of Rhodamine 6G solution containing powder sample **2** under UV irradiation. Irradiation duration, min.: 0 (curve 1); 5 (curve 2); 10 (curve 3); 15 (curve 4); 20 (curve 5); 25 (curve 6); 30 (curve 7); (**b**) kinetics of dye photodecomposition under UV radiation in solutions containing powder samples **1** (curve 1); **2** (curve 2); **3** (curve 3); **4** (curve 4); (**c**) dependencies 1/C = f(t) drawn for the dye photodecomposition in solutions containing powder samples.

The kinetic equation of pseudo-first order which is often used in the photocatalysis in integral form can be written as [13,74–76]:

$$\frac{C}{C_0} = e^{-kt} \tag{2}$$

where **$C_0$** and C—initial and current dye concentrations; (mM), **$t$**—duration of UV irradiation (min) and **$k$**—reaction rate constant (min$^{-1}$).

Figure 5b demonstrates kinetic dependencies of the dye photodecomposition in the solutions containing addition of different prepared composites. It can be seen that exper-

imental dates are sufficiently ($R^2 > 0.9$) described by exponential dependencies only for samples **1** and **4**, which demonstrate the relatively low effectiveness of dye photodecomposition (curves 1 and 4, Figure 5b). Experimental results of the dye photodecomposition in solutions containing samples **2** and **3** are poorly ($R^2 < 0.9$) described by exponential dependences.

In [77], the kinetic model of the pseudo-second order of the photocatalysis reaction rate was used. The kinetic equation in this model describes the linear dependence **1/C = *f(t)*** [77]:

$$\frac{1}{C} = \frac{1}{C_0} + k_2 \times t, \tag{3}$$

where $k_2$—constant of the photochemical reaction rate of pseudo-second order. Figure 5c present plots **1/C = *f* (t)** drawn for the dye photodecomposition in solutions containing powder samples. Pseudo-second order kinetics model somewhat better than pseudo-first order model corresponds to experimental data.

### 3.6. Adsorption Kinetics

It is known that the pollution adsorption plays an important role in a photocatalytic process [30]. Figure 6a demonstrates the kinetic dependencies of the dye adsorption from solutions on surfaces of powder samples.
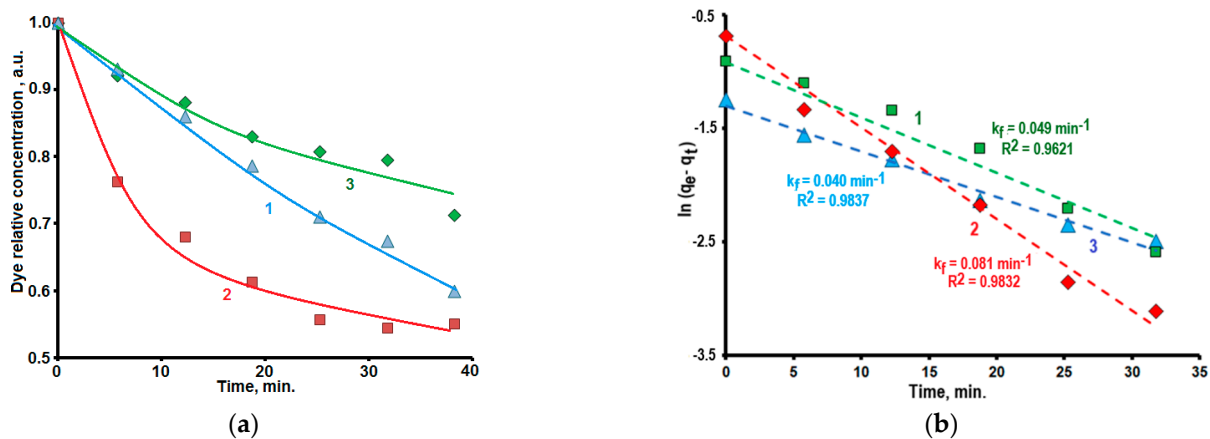


**Figure 6.** (**a**) Kinetic dependencies of the dye adsorption from solutions on surfaces of powder samples **2** (curve 1), **3** (curve 2), **4** (curve 3). (**b**) Dependencies $ln(q_e - q_t) = f(t)$ which were obtained from experimental data for the dye adsorption on the surfaces of powder samples **2** (curve 1), **3** (curve 2), **4** (curve 3).

The adsorption kinetics on the surface of solid materials often described using the Lagergren's model [78] and the corresponding equation which can be written in the integral form as:

$$ln(q_e - q_t) = ln\, q_e - k_f t, \tag{4}$$

where $q_t$ (mmol/g)—the current amount of dye adsorbed by 1 g of adsorbent up to time *t*; $q_e$—equilibrium adsorption capacity of the adsorbent; $k_f$ ($min^{-1}$)—adsorption rate constant; *t*—adsorption duration (min). According to (4), the adsorption rate decreases as the adsorbent surface is filled with dye molecules.

Figure 6b demonstrates dependencies **$ln(q_e - q_t) = f(t)$** calculated based on experimental data. The experimental data are close to linear dependencies and are described sufficiently ($R^2 > 0.96$) by the Equation (4).

The adsorption proceeds faster on the surface of samples **2** and **3** comparing with the adsorption on the sample **4**. The comparison of Figures 5b and 6a shows the similarity of the influence of $Fe_2O_3$ additions on kinetic dependencies of the dye adsorption and its

photodecomposition. Similar phenomenon was observed earlier for kinetics of the different dyes adsorption and photodecomposition by Cr-doped ZnO nanorods [79].

## 4. Discussion

Non-isothermal polymer-salt method was successfully applied to the synthesis of photoactive $ZnO-SnO_2-Fe_2O_3$ composites consisting of different oxide crystals. The data of SEM analysis show the presence of flower-like aggregates composed of hexagonal ZnO crystals in the structure of $ZnO-SnO_2-Fe_2O_3$ composites. Based on the results of DTA/TG analysis, we can suggest that the formation of the observed "flowers" can be related to the heterogeneous ZnO crystallization on oxide nanoparticles which could form faster than other during the non-isothermal thermal treatment.

The study has showed that obtained oxide composites demonstrate the ability of the chemically active singlet oxygen photogeneration. It is worth to notice that the photogeneration of singlet oxygen is observed under visible irradiation. This fact indicates the possibility of composites application to the air and water cleaning using the visible irradiation.

Obtained experimental results showed (Figure 5a, curves 2 and 3) that small $Fe_2O_3$ additions into $ZnO-SnO_2$ composites provide significant acceleration of the dye decomposition. This phenomenon could have been attributed to some changes of the electronic structures and optical properties of these composites. The band gap value $E_g$ of $Fe_2O_3$ is $2.0 \div 2.1$ eV [80,81] that is remarkably less than $E_g$ of ZnO or $SnO_2$ (~3.4 eV [40,42,82] and 3.6 eV [82], correspondingly). The addition of $Fe_2O_3$ can decrease the band gap value of composites [83] and increases the visible light absorption of composites [8]. High photocatalytic properties of $SnO_2/\alpha-Fe_2O_3$ and $ZnO/\alpha-Fe_2O_3$ heterostructures were described earlier in [8,26].

Changes in the electronic structure of $ZnO-SnO_2$ materials at the addition of Fe compounds play an important role in the observed high photocatalytic activity of $ZnO-SnO_2-Fe_2O_3$ composites prepared in this work. However, Figure 5b shows that composite **4** containing 10 mol. % of $Fe_2O_3$ demonstrate lower photocatalytic properties than composites **2** and **3** with lower content of $Fe_2O_3$. This phenomenon could be related to the difference of the materials structure and morphology so as to some features of the interactions between Rhodamine 6G molecules and the surface of prepared composites. In particular, the features of the interaction of dyes molecules with the surface of the photocatalytic material determine the significant differences of the photodecomposition and adsorption kinetics observed for different dyes [79]. Moreover, it was found [84] that the molecular structure of dyes and their interaction with the surface of photocatalytic material played a key role in visible-light photodegradation reactions on $F-TiO_2$ particles.

Moreover, according to XRD data (Figure 2), obtained composites also contain, besides ZnO, $SnO_2$, and $Fe_2O_3$, the crystals $ZnFe_2O_4$ and $ZnSnO_3$. The band gap of $ZnFe_2O_4$ crystals is ~1.9 eV [85] and this material demonstrates high photocatalytic properties. Therefore, the correct analysis of the influence of Fe compounds on the electronic structure of the prepared composites requires additional study in future.

The study of adsorption activity of the prepared composites suggests that observed high photocatalytic properties of $ZnO-SnO_2-Fe_2O_3$ composites with small (0.5 and 2.0 mol.%) content of $Fe_2O_3$ are significantly related to the features of their morphologies providing fast adsorption of dye molecules from the solutions.

**Author Contributions:** Conceptualization, S.K.E.; methodology, I.K.M.; validation, L.L.K.; formal analysis, D.V.B.; investigation, D.P.D.; data curation, D.P.D.; writing—original draft preparation, S.K.E. All authors have read and agreed to the published version of the manuscript.

**Informed Consent Statement:** Not applicable.

# References

1. Mediouni, N.; Guillard, C.; Dappozze, F.; Khrous, L.; Parola, S.; Colbeau-Juatin, C.; Ben Haj Amara, A.; Ben Rhaiem, H.; Jaffresic-Renault, N.; Namour, P. Impact of structural defects on the photocatalytic properties of ZnO. *J. Hazard. Mater. Adv.* **2022**, *6*, 100081. [CrossRef]
2. Das, A.; Wary, R.R.; Nair, R.G. Mn-doped ZnO: Role of morphological evolution on enhanced photocatalytic performance. *Energy Rep.* **2020**, *6*, 737–741. [CrossRef]
3. Das, A.; Malakar, P.; Nair, R.G. Engineering of ZnO nanostructures for efficient solar photocatalysis. *Mater. Lett.* **2018**, *219*, 76–80. [CrossRef]
4. Louis, J.; Padmanabhan, N.T.; Jayraj, M.K.; John, H. Crystal lattice engineering in a screw-dislocated ZnO nanocone photocatalyst by carbon doping. *Mater. Adv.* **2022**, *3*, 4322–4333. [CrossRef]
5. Pivert, M.L.; Poupart, R.; Capochichi-Gnambodoe, M.; Martin, N.; Leprince-Wang, Y. Direct growth of ZnO nanowires on civil engineering materials: Smart materials for supported photodegradation. *Microsyst. Nanoeng.* **2019**, *5*, 57. [CrossRef]
6. Laurent, K.; Brouri, A.; Capo-Chichi, M.; Yu, D.; Leprince-Wang, Y. Study on the structural and physical properties of ZnO nanowire arrays grown via electrochemical and hydrothermal depositions. *J. Appl. Phys.* **2011**, *110*, 094310. [CrossRef]
7. Kumar, P.; Khatri, T.; Bawa, H.; Kaur, J. ZnO-Fe$_2$O$_3$ heterojunction for photocatalytic degradation of Victoria blue dye. *AIP Proc.* **2017**, *1860*, 020065. [CrossRef]
8. Cheng, L.; Liu, L.; Li, R.; Zhang, J. Liquid phase deposition of $\alpha$-Fe$_2$O$_3$-ZnO heterojunction film with enhanced visible-light photoelectrocatalytic activity for pollutant removal. *J. Electrochem. Soc.* **2017**, *164*, H726. [CrossRef]
9. Hamrouni, A.; Moussa, N.; Parrino, F.; Di Paola, A.; Houas, A.; Palmisano, L. Sol-gel synthesis and photocatalytic activity of ZnO-SnO$_2$ nanocomposites. *J. Mol. Catal. A Chem.* **2014**, *390*, 133–141. [CrossRef]
10. Lamba, R.; Umar, A.; Mehta, S.K.; Kansal, S.K. Well-crystalline porous ZnO-SnO$_2$ nanosheets: An effective visible-light driven photocatalyst and highly sensitive smart sensor material. *Talanta* **2015**, *131*, 490–498. [CrossRef]
11. Evstropiev, S.K.; Karavaeva, A.V.; Petrova, M.A.; Nikonorov, N.V.; Vasilyev, V.N.; Lesnykh, L.L.; Dukelskii, K.V. Antibacterial effect of nanostructured ZnO-SnO$_2$ coatings: The role of microstructure. *Mater. Today Commun.* **2019**, *21*, 100628. [CrossRef]
12. Wang, C.; Wang, X.; Xu, B.-Q.; Zhao, J.; Mai, B.; Peng, P.; Sheng, G.; Fu, J. Enhanced photocatalytic performance of nanosized coupled ZnO/SnO$_2$ photocatalysts for methyl orange degradation. *J. Photochem. Photobiol. A Chem.* **2004**, *168*, 47–52. [CrossRef]
13. Evstropiev, S.K.; Lesnykh, L.L.; Karavaeva, A.V.; Nikonorov, N.V.; Oreshkina, K.V.; Mironov, L.Y.; Maslennikov, S.Y.; Kolobkova, E.V.; Vasilyev, V.N.; Bagrov, I.V. Intensification of photodecomposition of organic contaminations by nanostructured ZnO-SnO$_2$ coatings prepared by polymer-salt method. *Chem. Eng. Process. Process Intensif.* **2019**, *142*, 107587. [CrossRef]
14. Miao, Y.; Zhang, H.; Yuan, S.; Jiao, Z.; Zhu, X. Preparation of flower-like ZnO architectures assembled with nanosheets for enhanced photocatalytic activity. *J. Colloid Interface Sci.* **2016**, *462*, 9–10. [CrossRef]
15. Choudhary, S.; Sahu, K.; Bisht, A.; Satpati, B.; Mohapatra, S. Rapid synthesis of ZnO nanowires and nanoplates with highly enhanced photocatalytic performance. *Appl. Surf. Sci.* **2021**, *541*, 148484. [CrossRef]
16. Zhao, X.; Lou, F.; Li, M.; Lou, X.; Li, Z.; Zhou, J. Sol-gel-based hydrothermal method for the synthesis of 3D flower-like ZnO sheets for photocatalytic applications. *Ceram. Int.* **2014**, *40*, 5507–5511. [CrossRef]
17. Sun, Y.; Chen, L.; Bao, Y.; Zhang, Y.; Wang, J.; Fu, M.; Wu, J.; Ye, D. The applications of morphology controlled ZnO in catalysis. *Catalysts* **2016**, *6*, 188. [CrossRef]
18. Bora, T.; Sathe, P.; Laxman, K.; Dobretsov, S.; Dutta, J. Defect engineered visible light active ZnO nanorods for photocatalytic treatment of water. *Catal. Today* **2017**, *284*, 11–18. [CrossRef]
19. Shelemanov, A.A.; Evstropiev, S.K.; Karavaeva, A.V.; Nikonorov, N.V.; Vasilyev, V.N.; Podruhin, Y.F.; Kiselev, V.M. Enhanced singlet oxygen generation by bactericidal ZnO-MgO-Ag nanocomposites. *Mater. Chem. Phys.* **2022**, *276*, 125204. [CrossRef]
20. Vu, N.-N.; Kaliaguine, S.; Do, T.-O. Critical aspects and recent advances in structural engineering of photocatalysts for sunlight-driven photocatalytic reduction of CO$_2$ into fuels. *Adv. Funct. Mater.* **2019**, *29*, 1901825. [CrossRef]
21. He, Q.; Viengkeo, B.; Zhao, X.; Qin, Z.; Zhang, J.; Yu, X.; Hu, Y.; Huang, W.; Li, Y. Multiscale structural engineering of carbon nitride for enhanced photocatalytic H$_2$O$_2$ production. *Nano Res.* **2021**. [CrossRef]
22. He, Y.; Lei, Q.; Li, C.; Han, Y.; Shi, Z.; Feng, S. Defect engineering of photocatalysts for solar-driven conversion of CO$_2$ into valuable fuels. *Mater. Today* **2021**, *50*, 358–384. [CrossRef]
23. Zhang, Y.; Zhou, J.; Cai, W.; Zhou, J.; Li, Z. Enhanced photocatalytic performance and degradation pathway of Rhodamine B over hierarchical double-shelled zinc nickel oxide hollow sphere heterojunction. *Appl. Surf. Sci.* **2018**, *430*, 549–560. [CrossRef]
24. Song, X.; Jiang, W.; Cai, Z.; Yue, X.; Chen, X.; Dai, W.; Fu, X. Visible light-driven deep oxidation of NO and its durability over Fe doped BaSnO$_3$: The NO$^+$ intermediates mechanism and the storage capacity of Ba ions. *Chem. Eng. J.* **2022**, *444*, 136709. [CrossRef]
25. Zhang, H.; Yang, D.; Ji, Y.; Ma, X.; Xu, J.; Que, D. Low temperature synthesis of flowerlike ZnO nanostructures by cetyltrimethylammonium bromide-assisted hydrothermal process. *J. Phys. Chem. B* **2004**, *108*, 3955–3958. [CrossRef]
26. Kang, J.; Kuang, Q.; Xie, Z.-X.; Zheng, L.-S. Fabrication of SnO$_2$/$\alpha$-Fe$_2$O$_3$ hierarchical heterostructure and its enhanced photocatalytic property. *J. Phys. Chem. C* **2011**, *115*, 7874–7879. [CrossRef]
27. Heo, Y.W.; Norton, D.P.; Tien, L.C.; Kwon, Y.; Kang, B.S.; Ren, F.; Pearton, S.J.; La Roche, J.R. ZnO nanowire growth and devices. *Mater. Sci. Eng. R Rep.* **2004**, *47*, 1–47. [CrossRef]

28. Liang, Y.; Guo, N.; Li, L.; Li, R.; Ji, G.; Gan, S. Fabrication of porous 3D flower-like Ag/ZnO heterostructure composites with enhanced photocatalytic performance. *Appl. Surf. Sci.* **2015**, *332*, 32–39. [CrossRef]

29. Chakraborty, A.; Samriti; Ruzimuradov, O.; Gupta, R.K.; Cho, J.; Prakash, J. TiO$_2$ nanoflower photocatalysts: Synthesis, modifications and applications in wastewater treatment for removal of emerging organic pollutants. *Environ. Res.* **2022**, *212*, 113550. [CrossRef]

30. Uribe-López, M.C.; Hidalgo-López, M.C.; López-Gonsález, R.; Frías-Márquez, D.M.; Núñez-Noguera, G.; Hernández-Castillo, D.; Alvarez-Lemus, M.A. Photocatalytic activity of ZnO nanoparticles and the role of the synthesis method on their physical and chemical properties. *J. Photochem. Photobiol. A Chem.* **2020**, *404*, 112866. [CrossRef]

31. Zhang, L.; Jaroniec, M. Fundamentals of adsorption for photocatalysis. Chapter 2. *Interface Sci. Technol.* **2020**, *31*, 39–62.

32. Li, D.; Haneda, H.; Labhsetwar, N.K.; Hishita, S.; Ohashi, N. Visible-light-driven photocatalysis on fluorine-doped TiO$_2$ powders by the creation of surface oxygen vacancies. *Chem. Phys. Lett.* **2005**, *401*, 579–584. [CrossRef]

33. Bai, X.; Wang, L.; Zong, R.; Lv, Y.; Sun, Y.; Zhu, Y. Performance enhancement of ZnO photocatalyst via synergic effect of surface oxygen defect and grapheme hybridization. *Langmuir* **2013**, *29*, 3097–3105. [CrossRef]

34. Song, C.; Sun, Y.; Xu, Y.; Wang, D. Synthesis and optical property of ZnO nano-/micro-rods. *Front. Optoelectron. China* **2011**, *4*, 156–160. [CrossRef]

35. Choi, H.; Antoniou, M.G.; Pelaez, M.; de la Cruz, A.A.; Shoemaker, J.A.; Dionysiou, D.D. Mesoporous nitrogen-doped TiO$_2$ for the photocatalytic destruction of the a cyanobacterial toxin Microcyctin-LR under visible light irradiation. *Environ. Sci. Technol.* **2007**, *41*, 7530–7535. [CrossRef] [PubMed]

36. Li, R.; Zhang, L.; Wang, P. Rational design of nanomaterials for water treatment. *Nanoscale* **2015**, *7*, 17167–17194. [CrossRef] [PubMed]

37. Poongodi, G.; Anandan, P.; Mohan Kumar, R.; Jaya, R. Studies on visible light photocatalytic and antibacterial activities of nanostructured cobalt doped ZnO thin films prepared by sol-gel spin coating method. *Spectrochim. Acta Part A Molec. Biomolec. Spectr.* **2015**, *148*, 237–243. [CrossRef] [PubMed]

38. Byrne, C.; Subramanian, G.; Pillai, S.C. Recent advances in photocatalysis for environmental applications. *J. Environ. Chem. Eng.* **2018**, *6*, 3531–3555. [CrossRef]

39. Islam, M.R.; Rahman, M.; Farhad, S.F.U.; Podder, J. Structural, optical and photocatalysis properties of sol-gel deposited Al-doped ZnO thin films. *Surf. Interfaces* **2019**, *16*, 120–126. [CrossRef]

40. Davis, K.; Yarbrough, R.; Froeschle, M.; White, J.; Rathnayke, H. Band gap engineering zinc oxide nanostructures via a sol-gel synthesis of solvent driven shape-controlled crystal growth. *RCS Adv.* **2019**, *9*, 14638.

41. Zhu, L.-Y.; Yuan, K.-P.; Yang, J.-H.; Hang, C.-Z.; Ma, H.-P.; Ji, X.-M.; Devi, A.; Lu, H.-L.; Zhang, D.W. Hierarchical highly ordered SnO$_2$ nanobowl branched ZnO nanowires for ultrasensitive and selective hydrogen sulfide gas sensing. *Microsyst. Nanoeng.* **2020**, *6*, 30. [CrossRef] [PubMed]

42. Debanath, M.K.; Karmakar, S. Study of blue shift of optical band gap in zinc oxide (ZnO) nanoparticles prepared by low-temperature wet chemical method. *Mater. Lett.* **2013**, *111*, 116–119. [CrossRef]

43. Alibe, I.M.; Matori, K.A.; Sidek, H.A.A.; Yaakob, Y.; Rashid, U.; Alibe, A.M.; Zaid, M.H.M.; Nasir, S.; Nasir, M.M. Effect of polyvinylpyrrolidone on structural and optical properties of willemite semiconductor nanoparticles by polymer thermal treatment method. *J. Therm. Anal. Calorim.* **2019**, *136*, 2249–2268. [CrossRef]

44. Plakhova, T.V.; Shestakov, M.V.; Baranov, A.N. Effect of textured seeds on the morphology and optical properties of solution- and vapor-grown ZnO nanorod arrays. *Inorg. Mater.* **2012**, *48*, 469–475. [CrossRef]

45. Pachauri, V.; Subramaniam, C.; Pradeep, T. Novel ZnO nanostructures over gold and silver nanoparticles assemblies. *Chem. Phys. Lett.* **2006**, *423*, 240–246. [CrossRef]

46. Wang, X.; Ahmad, M.; Sun, H. Three-dimensional ZnO hierarchical nanostructures: Solution phase synthesis and applications. *Materials* **2017**, *10*, 1304. [CrossRef] [PubMed]

47. Qin, J.; Weng, B.; Zhao, L.; Chang, C.; Shi, Z.; Li, X.; Kim, H.-K.; Hwang, Y.-H. Synthesis and characterization of flower-like bundles of ZnO nanosheets by a surfactant-free hydrothermal process. *J. Nanomater.* **2014**, *2014*, 211. [CrossRef]

48. Kitabayashi, S.; Koga, N. Thermal decomposition of tin (II) oxyhydroxide and subsequent oxidation in air: Kinetic deconvolution of overlapping heterogeneous processes. *J. Phys. Chem. C* **2015**, *119*, 16188–16199. [CrossRef]

49. Toshiro, D.; Yoshio, N. Formation and behavior of singlet molecular oxygen in TiO$_2$ photocatalysis studied by detection of near-infrared phosphorescence. *J. Phys. Chem. C* **2007**, *111*, 4420–4424.

50. Kiselev, V.M.; Kislyakov, I.M.; Burchinov, A.N. Generation of singlet oxygen on the surface of metal oxides. *Opt. Spectrosc.* **2016**, *120*, 520–524. [CrossRef]

51. Bain, A.J.; Chandra, P.; Butcher, G.; Bryant, J. Picosecond polarized fluorescence studies of anisotropic fluid media. II. Experimental studies of molecular order and motion in jet aligned rhodamine 5G and resorufin solutions. *J. Chem. Phys.* **2000**, *112*, 10435–10449. [CrossRef]

52. Choi, W.K.; Sung, H.; Kim, K.H.; Cho, J.S.; Choi, S.C.; Jung, H.J.; Koh, S.K.; Lee, S.M.; Jeong, K. Oxidation process from SnO to SnO$_2$. *J. Mater. Sci. Lett.* **1997**, *16*, 1551–1554. [CrossRef]

53. Kanungo, S.B.; Mishra, S.K. Thermal dehydration and decomposition of FeCl$_{3-x}$H$_2$O. *J. Therm. Anal.* **1996**, *46*, 147–150. [CrossRef]

54. Rao, V.; Latha, P.; Ashokan, P.V.; Shridhar, M.H. Thermal degradation of poly(N-vinylpyrrolidone)-poly(vinyl alcohol) blends. *Polym. J.* **1999**, *31*, 887–889. [CrossRef]

55. Borodko, Y.; Lee, H.S.; Joo, S.H.; Zhang, Y.; Somorja, G. Spectroscopic study of the thermal degradation of PVP-capped Rh and Pt nanoparticles in $H_2$ and $O_2$ environments. *J. Phys. Chem. C* **2010**, *114*, 1117–1126. [CrossRef]
56. Lou, X.; Jia, X.; Xu, J.; Lin, S.; Gao, Q. Hydrothermal synthesis, characterization and photocatalytic properties of $Zn_2SnO_4$ nanocrystal. *Mater. Sci. Eng. A* **2006**, *432*, 221–225. [CrossRef]
57. Jeronsia, J.E.; Joseph, L.A.; Jaculine, M.M.; Vinosha, P.A.; Das, S.J. Hydrothermal synthesis of zinc stannate nanopartcicles for antibacterial applications. *J. Taibah Univ. Sci.* **2016**, *10*, 601–606. [CrossRef]
58. Tan, B.; Toman, E.; Li, Y.; Wu, Y. Zinc stannate ($Zn_2SnO_4$) dye-sensitized solar cells. *J. Amer. Chem. Soc.* **2007**, *129*, 4162–4163. [CrossRef]
59. Song, S.; Yang, X.; Zhang, Y.; Zhang, F.; Ding, J.; Bao, J.; Gao, C. Enhanced photocatalytic activity of sponge-like $ZnFe_2O_4$ synthesized by solution combustion method. *Prog. Nat. Sci. Mater. Int.* **2012**, *22*, 639–643. [CrossRef]
60. Evstropiev, S.K.; Soshnikov, I.P.; Khrebtov, A.I. The formation of ZnO-based coatings from solutions containing high-molecular polyvinylpyrrolidone. *Techn. Phys. Lett.* **2016**, *42*, 468–470. [CrossRef]
61. Djuriśtić, A.B.; Leung, Y.H.; Tam, K.H.; Hsu, Y.F.; Ding, L.; Ge, W.K.; Zhong, Y.C.; Wong, K.S.; Chan, W.K.; Tam, H.L.; et al. Defect emissions in ZnO nanostructures. *Nanotechnology* **2007**, *18*, 095702.
62. Vempati, S.; Mitra, J.; Dawson, P. One-step synthesis of ZnO nanosheets: A blue-white fluorophore. *Nanoscale Res. Lett.* **2012**, *7*, 470. [CrossRef] [PubMed]
63. Das, D.; Mondal, P. Photoluminescence phenomena prevailing in c-axis oriented intrinsic ZnO thin films prepared by RF magnetron sputtering. *RSC Adv.* **2014**, *4*, 35735–35743. [CrossRef]
64. Zhao, Y.; Cui, T.; Wu, T.; Jin, C.; Qiao, R.; Qian, Y.; Tong, G. Polymorphous ZnO nanostructures: Zn polar surface-guided size and shape evolution mechanism and enhanced photocatalytic activity. *ChemCatChem* **2017**, *9*, 3180–3190. [CrossRef]
65. Chen, D.; Wang, Z.; Ren, T.; Ding, H.; Yao, W.; Zong, R.; Zhu, Y. Influence od defects on the photocatalytic activity of ZnO. *J. Phys. Chem. C* **2014**, *118*, 15300–15307. [CrossRef]
66. Zeng, H.; Duan, G.; Li, Y.; Yang, S.; Xu, X.; Cai, W. Blue luminescence of ZnO nanoparticles based on non-equilibrium processes: Defect origins and emission controls. *Adv. Funct. Mater.* **2010**, *20*, 561–572. [CrossRef]
67. Kar, A.; Kundu, S.; Patra, A. Surface defect-related luminescence properties of $SnO_2$ nanorods and nanoparticles. *J. Phys. Chem. C* **2011**, *115*, 118–124. [CrossRef]
68. Chen, C.; Zhang, W.; Li, Y.; Cai, C. Defect-related optical bandgap narrowing and visible photoluminescence of hydrothermal-derived $SnO_2$ nanoparticles. *J. Mater. Sci. Mater. Electron.* **2017**, *28*, 18603–18609. [CrossRef]
69. Kamble, V.B.; Umarji, A.M. Defect induced optical bandgap narrowing in undoped $SnO_2$ nanocrystals. *AIP Adv.* **2013**, *3*, 082120. [CrossRef]
70. Jańczyk, A.; Krakowska, E.; Stochel, G.; Macyk, W. Singlet oxygen photogeneration at surface modified titanium dioxide. *J. Am. Chem. Soc.* **2006**, *128*, 15574–15575. [CrossRef]
71. Tamtaji, M.; Kazemeini, M. Enhanced singlet oxygen production under nanoconfinement using silica nanocomposites towards improving the photooxygenetion's conversion. *J. Nanoparticle Res.* **2022**, *24*, 174. [CrossRef]
72. Li, Y.; Zhang, W.; Niu, J.; Chen, Y. Mechanism of photogenerated reactive oxygen species and correlation with the antibacterial properties of engineered metal-oxide nanoparticles. *ACS Nano* **2012**, *6*, 5164–5173. [CrossRef] [PubMed]
73. Chen, X.; Wu, Z.; Liu, D.; Gao, Z. Preparation of ZnO photocatalyst for the efficient and rapid photocatalytic degradation of azo dyes. *Nanoscale Res. Lett.* **2017**, *12*, 143. [CrossRef] [PubMed]
74. Jin, C.; Ge, C.; Jian, Z.; Wei, Y. Facile synthesis and high photocatalytic degradation performance of $ZnO-SnO_2$ hollow spheres. *Nanoscale Res. Lett.* **2016**, *11*, 526. [CrossRef]
75. Liao, G.; He, W.; He, Y. Investigation of microstructure and photocatalytic performance of a modified zeolite supported nanocrystal $TiO_2$ composite. *Catalysts* **2019**, *9*, 502. [CrossRef]
76. Saratovskii, A.S.; Bulyga, D.V.; Evstrop'ev, S.K.; Antropova, T.V. Adsorption and photocatalytic activity of the porous glass-ZnO-Ag composite and ZnO-Ag nanopowder. *Glass Phys. Chem.* **2022**, *48*, 10–17. [CrossRef]
77. Irani, M.; Mohammadi, T.; Mohebbi, S. Photocatalytic degradation of Methulene Blue with ZnO nanoparticles; a joint experimental and theoretical study. *J. Mex. Chem. Soc.* **2016**, *60*, 218–225.
78. Lagergren, S.K. Zur theorie der sogenannten adsorption geloster stoffe. *Sevenska Vetensk. Handl.* **1898**, *24*, 39.
79. Chen, J.; Xiong, Y.; Duan, M.; Li, X.; Li, J.; Fang, S.; Qin, S.; Zhang, R. Insight into the synergistic effect of adsorption-photocatalysis for the removal of organic dye pollutants by Cr-doped ZnO. *Langmuir* **2020**, *36*, 520–533. [CrossRef]
80. Piccinin, S. The band structure and optical properties of hematite ($\alpha$-$Fe_2O_3$): A first principles GW-BSE study. *Phys. Chem. Chem. Phys.* **2019**, *21*, 2957–2967. [CrossRef]
81. Tahir, D.; Ilyas, S.; Rahmat, R.; Heryanto, H.; Fahri, A.N.; Rahmi, M.H.; Abdullah, B.; Hong, C.C.; Kang, H.J. Enhanced visible-light absorption of $Fe_2O_3$ covered by activated carbon for multifunctional purposes: Tuning the structural, electronic, optical, and magnetic properties. *ACS Omega* **2021**, *6*, 28334–28346. [CrossRef] [PubMed]
82. Kamarulzaman, N.; Kasim, M.F.; Rusdi, R. Band gap narrowing and widening of ZnO nanostructures and doped materials. *Nanoscale Res. Lett.* **2005**, *10*, 346. [CrossRef] [PubMed]
83. Liccardo, L.; Lushaj, E.; Compare, L.D.; Moretti, E.; Vomiero, A. Nanoscale ZnO/$\alpha$-$Fe_2O_3$ heterostructure: Toward efficient and low cost photoanodes for water splitting. *Small Sci.* **2022**, *2*, 2100104. [CrossRef]

84. Guo, J.; Yuan, S.; Jiang, W.; Yue, H.; Cui, Z.; Liang, B. Adsorption and photocatalytic degradation behaviors of rhodamine dyes on surface-fluorinated $TiO_2$ under visible irradiation. *RSC Adv.* **2016**, *6*, 4090–4100. [CrossRef]

85. Li, X.; Jin, B.; Huang, J.; Zhang, Q.; Peng, R.; Chu, S. $Fe_2O_3$/ZnO/$ZnFe_2O_4$ composites for the efficient photocatalytic degradation of organic dyes under visible light. *Solid State Sci.* **2018**, *80*, 6–14. [CrossRef]